arXiv:cond-mat/0302199v1 [cond-mat.supr-con] 11 Feb 2003

Anisotropic Vortex Pinning in Superconductors with a Square Array of Rectangular Submicron Holes

L. Van Look,[1] B. Y. Zhu,[1] R. Jonckheere,[2] B. R. Zhao,[3] Z. X. Zhao,[3] and V. V. Moshchalkov[1]
[1]*Laboratorium voor Vaste-Stoffysica en Magnetisme,*
K. U. Leuven
Celestijnenlaan 200 D, B-3001 Leuven, Belgium
[2]*Inter-University Micro-Electronics Center (Imec vzw), Kapeldreef 75, B-3001 Leuven, Belgium*
[3]*National Laboratory for Superconductivity, Institute of Physics and Center for Condensed Matter Physics,*
Chinese Academy of Sciences, Beijing 100080, China
(Dated: February 2, 2008)

We investigate vortex pinning in thin superconducting films with a square array of rectangular submicron holes (*"antidots"*). Two types of antidots are considered: antidots fully perforating the superconducting film, and *"blind antidots"*, holes that perforate the film only up to a certain depth. In both systems, we observe a distinct anisotropy in the pinning properties, reflected in the critical current I_c, depending on the direction of the applied electrical current: parallel to the long side of the antidots or perpendicular to it. Although the mechanism responsible for the effect is very different in the two systems, they both show a higher critical current and a sharper IV-transition when the current is applied along the long side of the rectangular antidots.

I. INTRODUCTION

Type-II superconductors (SC's) with nano-engineered artificial pinning arrays are good candidates to study the fundamentals of vortex pinning, since, within the limits of the lithographic process used for their fabrication, the pinning centers can be shaped and positioned in the SC at will. Often used systems in that respect are, for example, periodic arrays of submicron holes (antidots)[1,2,3,4,5] or magnetic dots, placed underneath or on top of the SC film[6,7,8,9,10].

In SC's with a periodic pinning array (PPA), so-called matching effects[2] occur, at specific magnetic fields generating a number of vortices which "matches" the number of available pinning sites. At these integer H_n and fractional $H_{p/q}$ matching fields, the vortices form regular geometrical patterns, commensurate with the pinning array. This strongly reduces the vortex mobility and consequently increases the critical current I_c. These commensurability effects have been recently intensively studied for square or triangular arrays of antidots[2,3,4] or magnetic dots[6,7,8].

In case of a square PPA, the equivalence between the two important in-plane directions, [10] and [01] (x- and y-axis), is conserved if square or cylindrical antidots (or out-of-plane magnetic dots) are used. However, as shown by recent numerical simulations, anisotropic pinning properties can be introduced in an otherwise isotropic superconducting film by using for example a *rectangular array* of *isotropic* pinning sites[11]. In the present work we study, by means of experiments and numerical simulations, the anisotropy in the pinning properties of a SC film caused by a *square array* of *rectangular antidots* and *blind antidots*.

This paper is organized as follows. First, we consider rectangular antidots that perforate the superconductor completely. For this system, we present experimental results and use numerical simulations to gain more insight in the mechanisms responsible for the observed anisotropy in the vortex mobility and dynamics. In a second part, we investigate rectangular antidots that do not perforate the superconducting film completely (*"blind antidots"*). Here, we will present only numerical simulations. Experiments on a square array of blind rectangular antidots have, to our knowledge, not been performed sofar.

II. SQUARE ARRAY OF RECTANGULAR ANTIDOTS

A. Electrical transport measurements

1. *Experimental details*

We patterned a SC Pb film in a 5×5 mm^2 cross-shaped geometry (see Fig. 1(a)) to allow electrical transport measurements in two perpendicular current directions. The central part of the cross consists of two 300 μm wide strips containing the square array of rectangular antidots (see dark gray area in Fig. 1(a)). In both strips, the long side of the antidots points in the y-direction. This pattern was prepared by electron-beam lithography in a polymethyl metacrylate/methyl metacrylate (PMMA/MMA) resist bilayer covering the SiO$_2$ substrate. A Ge(20 Å)/Pb(1500 Å)/Ge(300 Å) film was then electron-beam evaporated onto this mask while keeping the substrate at 77 K. After a liftoff process in warm acetone, the structure was covered with a thick insulating Ge(1000 Å) layer for protection against oxidation.

Figure 1(c) shows an atomic force microscopy (AFM) topograph of a 6×6 μm^2 area of the square antidot lattice with a period of 1.5 μm. We see that the antidots have a

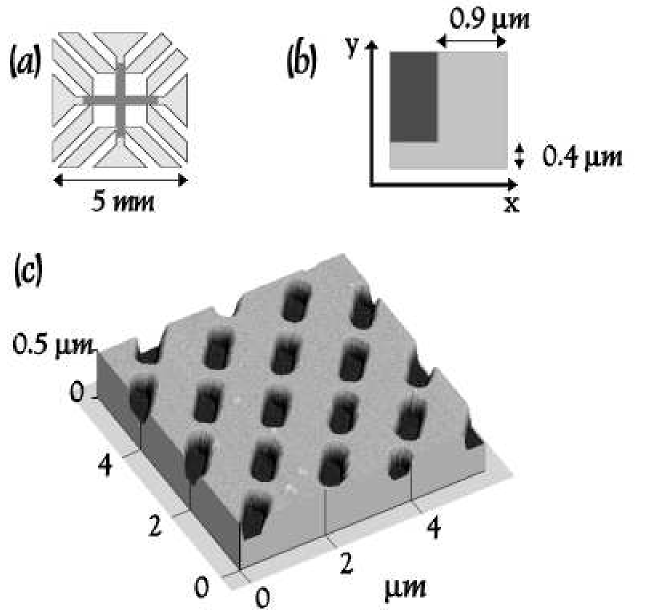

FIG. 1: Layout of the Pb film with a square array of rectangular antidots. (a) Cross-shaped geometry of the sample to allow for transport measurements in the x- and y-direction. (b) Schematic representation of a unit cell ($1.5 \times 1.5\ \mu\mathrm{m}^2$) of the antidot array. (c) Atomic force micrograph of a $6 \times 6\ \mu\mathrm{m}^2$ area of the antidot lattice.

rectangular shape ($0.6 \times 1.1\ \mu\mathrm{m}^2$) with rounded corners. As shown in the schematic representation of a unit cell of the array in Fig. 1(b), the superconducting paths between the antidots are 0.4 μm and 0.9 μm wide, for the x- and y-direction, respectively. The rms roughness value of the Ge/Pb/Ge film, in between the antidots, is less than 15 Å on a 1 $\mu\mathrm{m}^2$ area.

The transport measurements were performed in a ^{4}He cryostat equipped with a 9 T superconducting magnet. The magnetic field was applied perpendicular to the film surface. Four-point resistivity measurements were carried out using an ac bridge at a frequency of 19 Hz and a current of 10 μA. We obtained the superconducting critical temperature ($T_c = 7.26$ K) using a resistance criterion of 10 % of the normal state resistance R_n. The ratio of the R_n values for the x- and y-direction is

$$R_n^x/R_n^y = 1.06\ \Omega/0.46\ \Omega = 2.3,$$

which is in excellent agreement with the value 2.25 that can be expected from geometrical considerations. To determine the superconducting coherence length $\xi(0)$, we measured the linear $T_c(H)$ phase boundary of a co-evaporated reference film without any in-plane nanostructuring. From the $T_c(H)$ slope, and[12]

$$\mu_0 H_{c2} = \frac{\Phi_0}{2\pi\xi(T)^2} = \frac{\Phi_0}{2\pi\xi(0)^2}\left(1 - \frac{T}{T_c}\right), \qquad (1)$$

we find $\xi(0) = 51$ nm. Using the dirty limit ($\ell < \xi_0$) expression $\xi(0) = 0.865\sqrt{\xi_0 \ell}$ and the BCS coherence length for Pb, $\xi_0 = 83$ nm[13], we determined the elastic mean free path $\ell = 42$ nm. We can derive the penetration depth $\lambda(0) = 34$ nm by means of the dirty limit expression $\lambda(0) = 0.66\lambda_L\sqrt{\xi_0/\ell}$, using λ_L=37 nm as the London penetration depth[13]. Taking into account that the presence of antidots in a superconducting film has the tendency to increase the penetration depth in the following way[14]:

$$\Lambda(0) = \frac{\lambda(0)}{\sqrt{1 - 2\frac{S_a}{S_t}}} = 53\ \mathrm{nm}, \qquad (2)$$

where S_a is the area occupied by the antidots and S_t is the total area of the film, we obtain a Ginzburg-Landau (GL) parameter $\kappa = \Lambda(0)/\xi(0) \approx 1 > 1/\sqrt{2}$. We therefore conclude that the patterned film with the array of rectangular antidots is a type-II superconductor.

2. Results

In Fig. 2, we show the critical current versus field curves $I_c(H)$, normalized to its value at zero field, $I_{co} \equiv I_c(H = 0)$, at two temperatures ($T/T_c = 0.995$ in (a) and 0.992 in (b)). We have used a voltage criterion of $V_{crit} = 100\ R_n\ \mu\mathrm{V}/\Omega$, in order to be able to make a comparison between the two current directions with different normal state resistances R_n^x and R_n^y. The critical current density at zero field measured along the x-direction is $I_{co}^x = 4.4 \cdot 10^7 \frac{\mathrm{A}}{\mathrm{m}^2}$ at $T/T_c = 0.995$ and $I_{co}^x = 9.7 \cdot 10^7 \frac{\mathrm{A}}{\mathrm{m}^2}$ at $T/T_c = 0.992$. For a current along the y-direction, these values are $I_{co}^y = 1.3 \cdot 10^8 \frac{\mathrm{A}}{\mathrm{m}^2}$ at $T/T_c = 0.995$ and $I_{co}^y = 2.0 \cdot 10^8 \frac{\mathrm{A}}{\mathrm{m}^2}$ at $T/T_c = 0.992$. The field axis is given in units of the first matching field H_1, the field at which the density of ϕ_0-vortices equals the density of antidots: $\mu_0 H_1 = \Phi_0/d^2 = 9.2$ Oe, with $d = 1.5\ \mu$m the period of the antidot lattice and $\phi_0 = \frac{h}{2e}$ the superconducting flux quantum.

Due to the presence of the antidot lattice, both the $I_{cx}(H)$ and $I_{cy}(H)$ data show pronounced maxima at the integer matching fields H_1 and H_2 up to *the same critical current value.* The differences between the two current directions appear in the field ranges between the integer matching fields. For those field intervals, the critical current $I_{cy}(H)$ (filled symbols in Fig. 2) is considerably enhanced compared to $I_{cx}(H)$ (open symbols). This increase of I_{cy} is accompanied by the complete suppression of the rational matching peaks at $H_{p/q}$ (p and q integers). For $I_{cx}(H)$, on the other hand, the rational matching peaks at $H_{1/2}, H_{1/3}, H_{2/3}$ (panel (a)), and also at 3/2 H_1 (panel (b)) are clearly revealed.

To investigate the origin of this qualitative difference in the behavior of the critical currents along the two directions, we have a closer look at the $V(I_x)$ (open symbols) and $V(I_y)$ (solid lines) curves for some selected field values at $T/T_c = 0.995$ (Fig. 3). To make a comparison possible, the voltage axis is rescaled to $R_n I_{co}$, and the

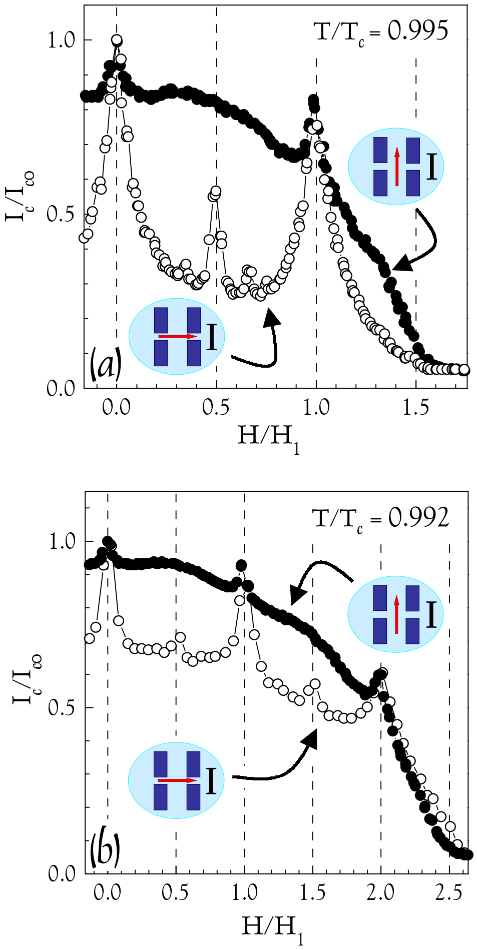

FIG. 2: Normalized critical currents I_{cx} and I_{cy} as a function of normalized magnetic field H/H_1 for the sample shown in Fig. 1 measured with a current in the x- (open symbols) and the y-direction (filled symbols), respectively. The $I_c(H)$ data are presented for two temperatures: (a) $T/T_c = 0.995$ and (b) $T/T_c = 0.992$.

current axis to I_{co}. The dotted horizontal line indicates the voltage criterium that was used to define the critical current shown in Fig. 2.

At $H = 0$ and $H = H_1$, the $V(I)$ transitions are very sharp and independent of the current direction. The $V(I_x)$ and $V(I_y)$ curves in Fig. 3 are therefore almost indistinguishable. At $H = H_1$, the appearance of a low-voltage tail in the $V(I)$ curve can be observed due to a small deviation from the first matching field. These $V(I)$ curves have a shape that is typical for a regular pinning array[15,16] as it was e.g. also observed in SC films with a periodically modulated thickness[17].

For $H = 0.4\ H_1$, the current at which the film completely reaches the normal state is the same for the two current directions, but a large tail in the $V(I_x)$ curve (open symbols) is present, indicating the dissipative motion of vortices in a direction perpendicular to the current. Consequently, the $V(I_x)$ transition is very broad (transition width $\Delta I = 0.8\ I_{co}$) compared to a much smaller broadening for $V(I_y)$ ($\Delta I = 0.2\ I_{co}$). This behavior is typical for every magnetic field in between the matching fields.

The field dependence of the transition width ΔI can be more adequately shown by presenting the $V(I_x, H)$ and $V(I_y, H)$ curves in a contour plot (Fig. 4(a) and (b)). We see that, at $H = 0$ and at $H = H_1$, the $V(I)$ transitions are equally sharp for both current directions. In between the integer matching fields, a substantial broadening of the $V(I_x)$ transition takes place (Fig. 4(a)). At the rational matching fields $H_{1/3}$, $H_{1/2}$, and $H_{2/3}$, the transitions regain part of their sharpness. For $I \parallel \mathbf{y}$ (Fig. 4(b)), all $V(I_y)$ curves, both at and in between the integer matching fields, have a sharp transition.

Summarizing the experimental observations, we have found a strong anisotropy in the critical current $I_c(H)$ and the $V(I)$ characteristics of a film with a square array of rectangular antidots. At the integer matching fields H_n, both the critical current $I_c(H_n)$ and the $V(I, H_n)$ curve do not depend on the direction of the applied current - $I \parallel \mathbf{x}$ or $I \parallel \mathbf{y}$. However, in between the integer matching fields, we find broad $V(I_x)$ transitions, a low I_{cx}, and rational matching features in $I_{cx}(H)$. For $I \parallel \mathbf{y}$, on the other hand, we see sharp $V(I_y)$ transitions at every magnetic field, an *overall* high I_{cy}, and no sign of rational matching features in $I_{cy}(H)$.

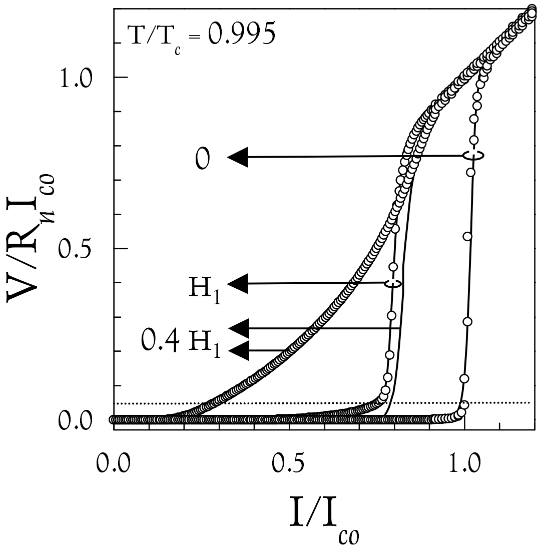

FIG. 3: Normalized $V(I)$ curves at selected magnetic field values at the same temperature ($T/T_c = 0.995$) as the measurements in Fig. 2(a). The full lines are the data for $I \parallel \mathbf{y}$, the open symbols for $I \parallel \mathbf{x}$. The horizontal dotted line indicates the voltage criterium used to define the critical current. For $H = 0$ and $H = H_1$, the curves for the two current directions overlap almost completely.

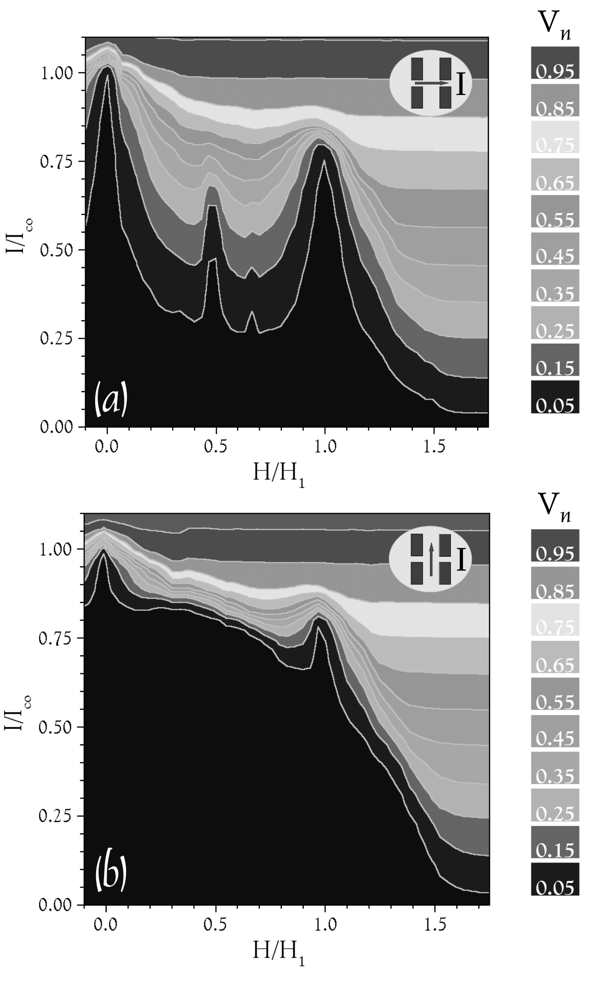

FIG. 4: Contour plots (a) $V(I_x, H)$ and (b) $V(I_y, H)$ at T/T_c = 0.995. The gray scale indicates the normalized voltage $V_n = \frac{V}{R_n I_{c0}}$. The evolution of the $V(I)$ transition width as a function of magnetic field can easily be seen from this plot.

3. Discussion

The differences between $I_{cx}(H)$ and $I_{cy}(H)$ are due to an anisotropy in the vortex mobility in the sample along the two in-plane directions. Neglecting the thermal noise force, the velocity $\mathbf{v}$ of a vortex in a PPA is determined by the superposition of three forces: the vortex-vortex interaction $\mathbf{F}_{VV}$, the vortex-antidot pinning force $\mathbf{F}_P$ and the Lorentz force $\mathbf{F}_L$, directed perpendicular to the applied current. The critical current I_c of the system is proportional to the Lorentz force $\mathbf{F}_L$ which is needed to induce a threshold average vortex velocity, and therefore a certain critical voltage. To reach this voltage, a noticeable fraction of the vortices must be depinned by the joint effect of the Lorentz $\mathbf{F}_L$ and the vortex-vortex interaction $\mathbf{F}_{VV}$ forces. The balance between these forces, and consequently I_c, depends strongly on the applied magnetic field, since the latter determines the density of vortices in the sample.

When, for example, all pinning sites in a square PPA are occupied by a vortex (first matching field H_1), the vortex lattice has such a high symmetry, that all vortex-vortex interactions between the vortices trapped in the pinning sites cancel out ($\mathbf{F}_{VV} = 0$). Therefore, at this field, the Lorentz force $\mathbf{F}_L$ which is needed for depinning, is only determined by the pinning force. This implies that the critical current at the first matching field $I_c(H_1)$ is a measure of the *single site pinning force* of the individual antidots. Once the Lorentz force exceeds the pinning force, all vortices leave their pinning site simultaneously, resulting in a sharp $V(I)$ transition[18].

Since the $I_{cx}(H_1)$ and $I_{cy}(H_1)$ values and the $V(I_x, H_1)$ and $V(I_y, H_1)$ curves (Figs. 2 and 3) coincide, we conclude that the pinning force exerted by a rectangular antidot on a single pinned ϕ_0-vortex is *isotropic* along the two symmetry-axes of the rectangular antidot. This experimental observation is in agreement with predictions by Buzdin and Daumens[19] for an elliptic antidot, where the pinning force is only expected to be anisotropic when the ellipse is extremely elongated.

The observed anisotropy in pinning properties can therefore *not* be attributed to an anisotropic single site pinning force of the rectangular antidots themselves, but rather to their arrangement in the array. In other words, *the observed anisotropy in the pinning properties should be associated with an anisotropic vortex-vortex interaction.* Indeed, since the SC strands between the antidots, where the screening currents of the vortices have to flow, are much thinner between the adjacent antidots in the y-direction than in the x-direction, we expect the y-component of the vortex-vortex interaction forces to be considerably larger than their x-component.

To understand how the anisotropic vortex-vortex interaction can give rise to the observed anisotropy in the pinning properties in between the matching fields, we examine the role of the vortex-vortex interaction in the depinning process of vortices in a regular pinning array.

We have discussed earlier that at a matching field, the vortex-vortex interaction vectors are canceled out and depinning is governed by the single site pinning force. When the applied field is now slightly detuned from a matching field (integer or rational), the vortex lattice contains defects due to the incommensurability of the vortex array and the PPA. The vortex rows, parallel to $\mathbf{F}_L$, without such defects are called “commensurate” rows. In these commensurate vortex rows, the component of $\mathbf{F}_{VV}$ parallel to $\mathbf{F}_L$ will be zero for all vortices in the row. On the other hand, in vortex rows containing defects, the vortex-vortex interaction forces will not cancel out at all ($\mathbf{F}_{VV} \neq 0$). This $\mathbf{F}_{VV}$ component in the direction of the Lorentz force $\mathbf{F}_L$ will assist to the depinning of these “incommensurate” rows, i.e. depinning occurs when the sum of this $\mathbf{F}_{VV}$ component and $\mathbf{F}_L$ overcomes the single site pinning force. The commensurate rows stay pinned up to a higher Lorentz force $\mathbf{F}_L$[20]. If the vortex-vortex interaction is sufficiently large, the critical current $I_c(H)$ will therefore be substantially lower right before and after the matching fields, leading to pronounced matching peaks (integer and rational).

When the current is applied in the x-direction ($\mathbf{F}_L \parallel \mathbf{y}$), the $I_{cx}(H)$ curve shows pronounced maxima at the rational matching fields $H_{1/2}$, $H_{3/2}$, $H_{1/3}$ and $H_{2/3}$ and a much lower value in between these rational matching fields (see Fig. 2). This is a clear sign of a strong vortex-vortex interaction $\mathbf{F}_{VV}$ component along the direction of the Lorentz force $\mathbf{F}_L$, in this case the y-direction.

When a current is applied in the y-direction ($\mathbf{F}_L \parallel \mathbf{x}$), we see a complete disappearance of the rational matching peaks and, instead, an overall high critical current $I_{cy}(H)$ (Fig. 2). This indicates that the $\mathbf{F}_{VV}$ components along the direction of the Lorentz force (in this case the x-direction) are much weaker than in the case $I \parallel \mathbf{x}$. The vortex-vortex interaction is apparently not able to provide the long-range order needed to generate the sparse geometrical patterns at the rational matching fields $H_{p/q}$. This implies that no commensurate rows in the direction of $\mathbf{F}_L$ are formed, and all vortex rows are qualitatively equal (all are "incommensurate"). All rows will depin approximately at the same driving current. This explains the sharp $V(I_y)$ transitions for all magnetic fields (see Fig. 4(b)). The integer matching peaks are still present in $I_{cy}(H)$, since the commensurate vortex patterns at the integer matching fields H_n can be achieved even with a small interaction force present, due to a smaller vortex separation.

Our critical current results are in agreement with what was found in phase boundary measurements on square SC networks with a different wire width in the two perpendicular directions[21]. In these systems, $T_c(H)$ depends on the direction of the current in a similar way as in our $I_c(H)$ data. This is not surprising since there are many similarities between SC films with an antidot lattice and SC wire networks, especially at temperatures close to T_c. Using the temperature to tune the coherence length $\xi(T)$, one can, in fact observe a weakly coupled network behavior ($\xi(T) \gg$ strips between the antidots) in any antidot array.

Summarizing this part of the discussion, our main experimental observations can be explained by (i) an *isotropic* single site pinning force of the rectangular antidots, combined with (ii) an *anisotropic* vortex-vortex interaction between the vortices trapped inside the antidots.

B. Numerical simulations

We have used molecular dynamics simulations to confirm that a model system with the features (i) and (ii) mentioned above, shows indeed the anisotropy in the critical current that was observed in the experiments.

1. Model

We consider a two-dimensional system with periodic boundary conditions containing a square array (period d) of circular (i.e. *isotropic*) pinning sites, but with an *anisotropic* vortex-vortex interaction. The overdamped equation of motion for a vortex i (Eq.(3)) is used to calculate the average vortex velocity as a function of the applied Lorentz force $\mathbf{F}_L$, and to trace the vortex trajectories in the pinning array:

$$\eta \mathbf{v}_i = \mathbf{F}_L + \mathbf{F}_{vv}(\mathbf{r}_i) + \mathbf{F}_p(\mathbf{r}_i), \qquad (3)$$

where η is the viscosity coefficient and taken to be unity. The driving force acting on the vortices is the Lorentz force, $\mathbf{F}_L = \mathbf{J} \times \phi_0$, where $\mathbf{J}$ is the applied current.

The *anisotropic* repulsive vortex-vortex interaction force between two vortices with separation r_{ij} is described by the modified Bessel function K_1[22,23,24,25]:

$$\mathbf{F}_{vv}(\mathbf{r}_i) = F_{vv0} f_0 \sum_{j \neq i}^{N_v} K_1\left(\frac{\mathbf{r}_i - \mathbf{r}_j}{\lambda}\right)\mathbf{r}_{ij}, \qquad (4)$$

where $\mathbf{r}_{ij} = \frac{(\mathbf{r}_i - \mathbf{r}_j)}{|\mathbf{r}_i - \mathbf{r}_j|}$, and N denotes the number of vortices in the sample. $F_{vv0} f_0$ expresses the intensity of the vortex-vortex interaction force, with $f_0 = \frac{\phi^2}{8\pi^2\lambda^3}$. The cut-off for the vortex-vortex interaction lies at 6 d in both the x- and the y-direction. The vortex-vortex interaction is made anisotropic by choosing $\lambda_y = 2\lambda_x = d$. All forces are expressed in units of f_0.

The rectangular antidots of the experiment are modeled as potential wells with an *isotropic* attractive pinning force $\mathbf{F}_p$ given by:

$$\mathbf{F}_p(\mathbf{r}) = -F_{p0} f_0 \sum_{k=1}^{N_p} \frac{\mathbf{r}}{R_p} exp\left(-\left|\frac{\mathbf{r}}{R_p}\right|^2\right), \qquad (5)$$

Here, $\mathbf{r}$ is the distance between the vortex and the k^{th} pinning site.

Calculations are performed on a square sample (side 8 d) with periodic boundary conditions in both x- and y-directions. The same initial vortex configuration, obtained from an annealing course[18], is used for the hysteretic calculation of the $\langle v \rangle (F_L)$ current-voltage characteristics along the x- and the y-direction.

We solve the equation of motion (Eq.(3)) by taking discrete time steps Δt, using the following fixed lengths and forces: $R_p = 0.7$, $\lambda_y = 6$, $F_{vv0} = 0.2$, $F_{p0} = 1$. The average vortex velocity as a function of applied driving force $\langle v \rangle (F_L)$ is obtained by increasing F_L in small steps $\Delta F_L = 0.001$, starting from $F_L = 0$. At each F_L, we neglect the first 2000 time steps, and average the next 8000 steps to calculate the average velocity of all the vortices in the system.

2. Results

The obtained average vortex velocity as a function of the applied Lorentz force for $H/H_1 = 0.58$, i.e. a magnetic field in between matching fields, is shown in Fig. 5. We will compare these calculated $\langle v\rangle(F_L)$ curves at $H/H_1 = 0.58$ with the experimental $V(I)$ curves taken at $H/H_1 = 0.4$ (Fig. 3), which are typical for all magnetic fields in between matching fields. The two main features observed in the experimental curves are qualitatively reproduced. First, the onset of the vortex motion occurs at lower driving force for $I \parallel \mathbf{x}$ ($\mathbf{F}_L \parallel \mathbf{y}$) (open symbols) than for $I \parallel \mathbf{y}$ ($\mathbf{F}_L \parallel \mathbf{x}$) (filled symbols). The critical depinning force in the y-direction lies at $F_L \approx 0.315$, while it is $F_L \approx 0.37$ when the force is applied in the x-direction. Therefore, the critical current for $I \parallel \mathbf{x}$ is lower than for $I \parallel \mathbf{y}$. Secondly, the $V(I)$ transition is clearly much broader for $I \parallel \mathbf{x}$ than for $I \parallel \mathbf{y}$, with a gradually increasing average vortex velocity.

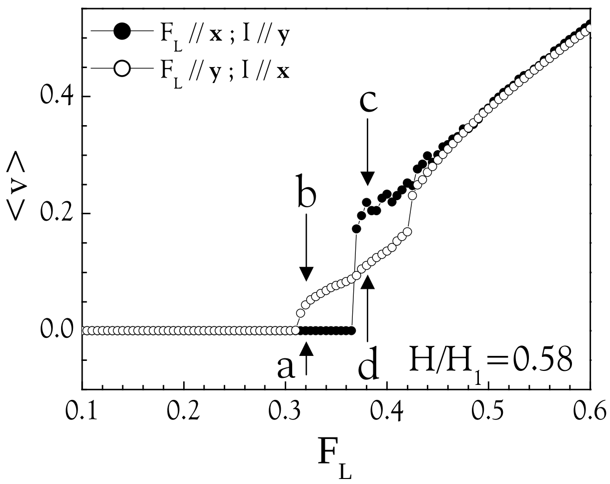

FIG. 5: Average vortex velocity as a function of the Lorentz force F_L at $H/H_1 = 0.58$. The open (filled) symbols show the result for a current along the x- (y-) axis. Arrows a and c (b and d) indicate the points at which the vortex trajectories for $I \parallel \mathbf{y}$ ($I \parallel \mathbf{x}$) were calculated, shown in Fig. 6.

The origin of the different $\langle v\rangle(F_L)$ behavior for the two directions of the Lorentz force can be found by examining the trajectories of the depinned vortices (Fig. 6) at two Lorentz force values, indicated by arrows in Fig. 5. A Lorentz force of 0.32, applied in the x-direction (arrow a in Fig. 5) is not sufficient to depin any vortex rows (see Fig. 6(a)). When the same $F_L = 0.32$ is applied in the y-direction (arrow b in Fig. 5), a *partial depinning* takes place, where the rows with little order in the y-direction (incommensurate rows) are the first ones to start moving (see Fig. 6(b)). The commensurate rows (the first, second, and forth row, counting from the left) remain pinned (see also Section II A 3). At a Lorentz force $F_L = 0.38$, applied along the x-direction (arrow c in Fig. 5), all the vortex rows have started to move (Fig. 6(c)). This corresponds to the sharp increase in $\langle v\rangle$ that can be found in the $\langle v\rangle(F_L)$ curve (filled symbols in Fig. 5). For the same $F_L = 0.38$ applied in the y-direction (arrow d in Fig. 5), the vortices in the incommensurate rows move with a higher velocity (Fig. 6(d)). When an even higher Lorentz force is applied (e.g. $F_L = 0.44$), all vortices finally move for both $\mathbf{F}_L$ directions (not shown).

3. Discussion

The results of these molecular dynamics simulations show that an array of *isotropic pinning sites*, combined with an *anisotropic vortex-vortex interaction* along the two principal axes of the PPA, gives rise to the same phenomena as observed in our pinning experiments on a Pb film with a square array of rectangular antidots. The low critical current and broad $V(I)$ transitions in between matching fields for $I \parallel \mathbf{x}$ ($\mathbf{F}_L \parallel \mathbf{y}$) are found to be due to the motion of the incommensurate vortex rows along the direction of the strong vortex-vortex interaction, in this case the y-direction. For $I \parallel \mathbf{y}$ ($\mathbf{F}_L \parallel \mathbf{x}$), the simultaneous vortex depinning at a relatively high driving force is responsible for the high critical current and the sharp $V(I)$ transitions. This result strengthens our interpretation that in our experiment, the rectangular antidots provide an *isotropic pinning potential* but induce an *anisotropy in the vortex-vortex interaction.*

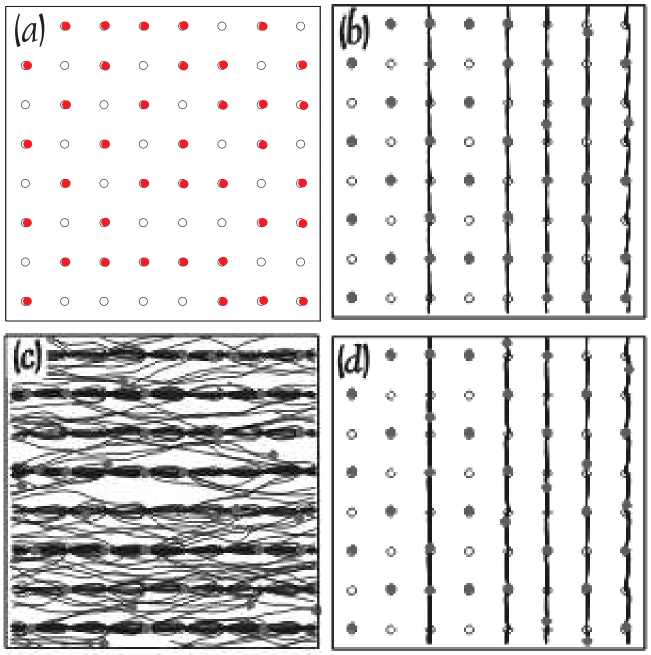

FIG. 6: Vortex trajectories (lines) for $H/H_1 = 0.58$ at $F_L = 0.32$ for a current in the y- (a) and the x-direction (b). Open circles represent pinning sites, black dots represent vortices. Idem at $F_L = 0.38$ for the current in the y- (c) and x-direction (d). The labels (a) to (d) correspond to the arrows in Fig. 5.

Due to the anisotropic nature of the vortex-vortex interaction, the initial vortex lattice found in the simulation by an annealing course shows more order in the y-direction (stronger vortex-vortex interaction) than in the x-direction (weaker vortex-vortex interaction) (see Fig. 6(a)). Although we believe that this is also what happens in the experiment, no definitive statement about the experimental vortex configuration can be made, however, at this stage, before a direct experimental study of the vortex patterns in these anisotropic pinning arrays, e.g. by scanning Hall probe[26,27] or Lorentz[28] microscopy.

It is interesting to compare our results with the molecular dynamics simulations on a *rectangular* array of isotropic pinning sites, recently performed by Reichhardt *et al.*[11]. In that case, the anisotropy in $\mathbf{F}_{VV}$ between pinned vortices is induced by a different spacing in the x- and y-direction of the pinning sites. A similar anisotropy in $I_c(H)$ as in our measurements and calculations is indeed found when no interstitial vortices are present ($H < H_1$). When the Lorentz force $\mathbf{F}_L$ is in the direction of the weak vortex-vortex interaction (in the case considered in Ref.[11] along the direction with a large lattice spacing) the absence of rational matching and an overall high $I_c(H)$ is found.

C. Summary

We have measured $I_c(H)$ and $V(I, H)$ curves of a SC film with a square array of rectangular antidots for two directions of the applied current. We find an *overall high* $I_c(H)$ with integer matching peaks but no rational matching features when the current is applied parallel to the long side of the antidots. This is a clear advantage compared to isotropic pinning arrays, where a large suppression of $I_c(H)$ is seen in between the rational matching fields. We attribute this effect to the *anisotropic vortex-vortex interaction*, which is stronger along the long side of the antidots. Molecular dynamics simulations on a square array of *isotropic* pinning sites, combined with an *anisotropic* vortex-vortex interaction, indeed show the same characteristic anisotropic features as observed in our measurements.

III. SQUARE ARRAY OF RECTANGULAR BLIND ANTIDOTS: NUMERICAL SIMULATIONS

In this Section, we examine the vortex mobility in a superconductor with a square array of rectangular *blind* antidots by means of molecular dynamics simulations. Blind antidots are holes that do not perforate the superconductor completely, i.e. the bottom of a blind antidot always contains superconducting material. Therefore, if more than one vortex is trapped inside a blind antidot, the vortices remain individual repulsive entities, without merging into one multiple-quantum vortex[3,29], as in the case of an antidot.

Moreover, a vortex trapped inside a blind antidot can move around freely within the boundaries of the pinning center. In a film with antidots, on the other hand, the supercurrents constituting the vortex are forced to flow at the outer edge of the antidot, confining the vortex in space.

A. Model

Taking into account the properties of a blind antidot, mentioned above, we will use the following model to simulate the vortex motion in a superconductor with an array of blind antidots.

Again, we use a square 2D system (size $8d$) with periodic boundary conditions in the x- and y-direction. The system contains a square array (period d) of rectangular pinning sites (sides $R_x = 0.4d$ and $R_y = 0.77d$). The vortex velocities are calculated using the normalized overdamped equation of motion Eq. (3). The repulsive vortex-vortex interaction is described by Eq. (4), using an *isotropic* penetration depth $\lambda = d$ and $F_{vv0} = 0.2$.

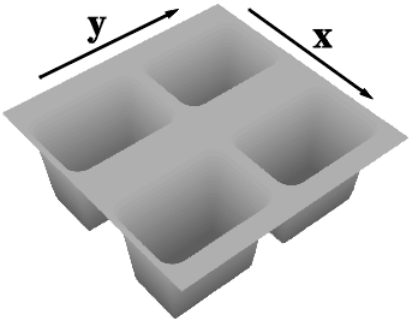

FIG. 7: 3D plot of the pinning potential used to model a square array of rectangular blind antidots.

The pinning force of a rectangular pinning center on the vortex can be defined as[22]:

$$\mathbf{F}_p(\mathbf{r}) = -F_{p0} f_0 \sum_{k=1}^{N_p} \frac{\mathbf{r}}{R_p} exp\left(-\left|\frac{\mathbf{r}}{R_p}\right|^2\right), \qquad (6)$$

when the vortex is outside the k^{th} rectangular pinning center, and $\mathbf{F}_p(\mathbf{r}) \equiv 0$, if the vortex is inside the rectangular area of the pinning site. This means that no pinning force is exerted on the vortex, once it is trapped inside the blind antidot. In this expression, $\mathbf{r}$ is the distance between the vortex and the edge of the k^{th} rectangular pinning center. We have chosen R_p to be $R_p = 0.067d$ and $F_{p0} = 1$. In Fig. 7, we show schematically the 3D pinning potential that was used for this simulation.

The current-voltage characteristics $\langle v \rangle (F_L)$ and the vortex trajectories for a current along the x- and the y-direction are calculated using the method described in Section II B 1.

B. Results and discussion

In Fig. 8, we show the calculated $\langle v\rangle(F_L)$ curves at $H/H_1 = 0.8$, for a driving force $\mathbf{F}_L$ in the x- (filled symbols) and the y-direction (open symbols). The magnetic field is chosen in between matching fields, where no commensurate vortex configuration can be established.

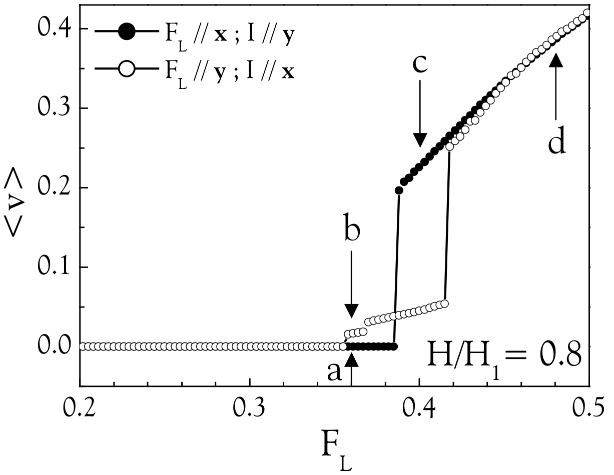

FIG. 8: Average vortex velocity as a function of the Lorentz force $\mathbf{F}_L$ at $H/H_1 = 0.8$. The open (filled) symbols show the result for a current along the x- (y-) axis. Arrows a and c (b and d) indicate the points at which the vortex trajectories for $I \parallel \mathbf{y}$ ($I \parallel \mathbf{x}$) were calculated, shown in Fig. 9.

The calculation shows that the onset of vortex motion occurs at a lower Lorentz force F_L when $\mathbf{F}_L \parallel \mathbf{y}$. For this direction of the driving force, the average vortex velocity becomes finite at $\mathbf{F}_L \approx 0.356$. When the Lorentz force is applied in the perpendicular direction ($\mathbf{F}_L \parallel \mathbf{x}$), vortex motion is delayed until $\mathbf{F}_L \approx 0.386$. Consequently, the critical current I_c is smaller for $I \parallel \mathbf{x}$ than for $I \parallel \mathbf{y}$.

Moreover, there is a striking difference in the width of the depinning transition. When $\mathbf{F}_L \parallel \mathbf{y}$, we observe several steps in the depinning process, leading to a broad transition, while for $\mathbf{F}_L \parallel \mathbf{x}$, the $\langle v\rangle(F_L)$ curve shows a single sharp jump at $F_L \sim 0.386$.

We examine the origin of this qualitatively different behavior for the two directions of the Lorentz force by plotting the vortex trajectories and positions after 10^5 time steps (see Fig. 9) at some specific Lorentz force values, indicated by arrows in Fig. 8.

First, we observe a different configuration of the pinned vortices in Fig. 9(a) and (b), although they originate from the same annealing course. The difference results from vortex jumps that occur after the annealing course, under the influence of the applied Lorentz force. These jumps aid the system to obtain its lowest energy configuration. At a magnetic field of $H/H_1 = 0.8$, it is not possible to obtain a completely regular vortex pattern. The commensurate configuration, which is closest to $0.8H_1$ is $0.75H_1 = H_{3/4}$, where one finds consecutively completely filled rows and rows with half-filling. At $H/H_1 = 0.8$, the energetically most favorable vortex configuration looks like the configuration at $H_{3/4}$, but with some excess vortices that are placed in the rows with half-filling. Because the jumps are assisted by the Lorentz force, we find this kind of order in the vortex positions only in the direction of the applied Lorentz force (along the x-direction in Fig. 9(a) and along the y-direction in Fig. 9(b)).

A Lorentz force of 0.36 applied in the x-direction (arrow a in Fig. 8 is not sufficient to depin any vortex rows (see Fig. 9(a)). When the same $F_L = 0.36$ is applied in the y-direction (arrow b in Fig. 8), a *partial depinning* takes place, where the row with the least order in the y-direction (the first vertical row counting from the right in Fig. 9(b)), is set in motion. The moving vortex row is the only one that contains 6 vortices. Accommodating these six vortices in a row of eight pinning sites gives rise to a lot of strain, making it considerably easier to depin this incommensurate row. Most of the other rows contain either eight or four vortices, which can be easily positioned in a low energy configuration (commensurate rows). One vertical row accommodates five vortices. This row will be the next to be depinned when the Lorentz force is increased (at $F_L \approx 0.37$), creating the second step in the $\langle v\rangle(F_L)$ curve for $\mathbf{F}_L \parallel \mathbf{y}$ in Fig. 8 (open symbols).

At a Lorentz force of $F_L = 0.4$, applied along the x-direction, all vortices are set in motion (Fig. 9(c)). This corresponds to the sharp increase in $\langle v\rangle$ that is seen in the $\langle v\rangle(F_L)$ curve (filled symbols in Fig. 8). When a Lorentz force of $F_L = 0.48$ is applied in the y-direction (arrow d

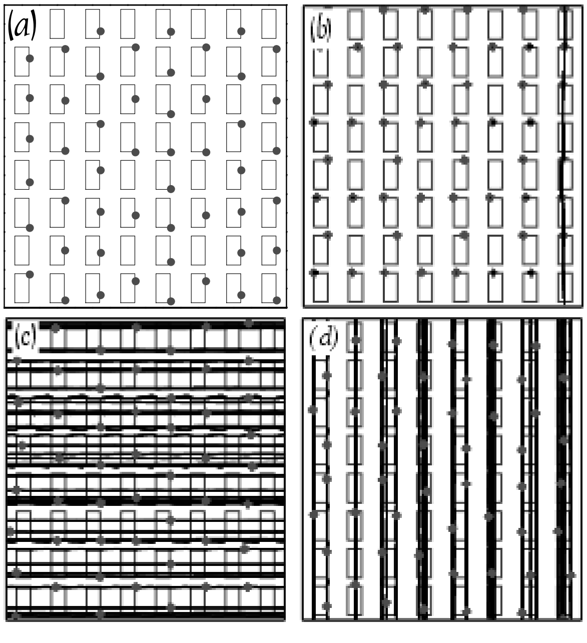

FIG. 9: Vortex trajectories (lines) for $H/H_1 = 0.8$ at $F_L = 0.36$ for a current in the y- (a) and x-direction (b). Rectangles represent the blind rectangular antidots, black dots represent vortices. Idem at $F_L = 0.40$ for a current in the y-direction (c), and at $F_L = 0.48$ for a current in the x-direction. The labels (a) to (d) correspond to the arrows in Fig. 8.

in Fig. 8), all vortices participate in the motion.

In Fig. 9(a), one also finds commensurate horizontal rows, containing eight or four vortices, one incommensurate horizontal row with five and one with six vortices. However, these incommensurate rows do not give rise to a partial depinning as in the case $\mathbf{F}_L \parallel \mathbf{y}$, because the strain that is caused by the incommensurability is effectively released by *shifting the vortex positions within the rectangular blind antidot.* When $\mathbf{F}_L \parallel \mathbf{x}$, the long side ($R_y$) of the rectangular blind antidot can be used for this purpose. For $\mathbf{F}_L \parallel \mathbf{y}$, the vortices are all located at the top edge of the rectangular antidots. Consequently, only the short side of the antidots (R_x) is available, resulting in large stresses in the incommensurate vertical rows which initiate the partial depinning proces.

We also notice that there is some amount of row switching at high driving force for $\mathbf{F}_L \parallel \mathbf{x}$ due to the smaller spacing between the blind antidots in that direction. Although the plotted trajectory lines in Fig. 9(c) do not show it directly, we know the switching takes place by comparing the number of vortices in a particular horizontal row at low and at high driving force. On the other hand, *no* row switching is seen when $\mathbf{F}_L \parallel \mathbf{y}$.

We have also examined the effect of the side ratio of the rectangular blind antidots R_y/R_x on the vortex depinning. In Fig. 10, we present $\langle v\rangle(F_L)$ curves (shifted vertically for clarity) at $H/H_1 = 0.8$ for various R_y/R_x, smaller than the ratio used for Fig. 8.

When $\mathbf{F}_L \parallel \mathbf{y}$ (Fig. 10(b)), the $\langle v\rangle(F_L)$ curves are almost independent on the ratio R_y/R_x. The transition is always a two-step process, involving partial depinning of the incommensurate vertical rows, as described above.

When $\mathbf{F}_L \parallel \mathbf{x}$ (Fig. 10(a)), we find a sharp depinning transition, resulting from simultaneous depinning of all vortices and a high critical current, if R_y is sufficiently large, $R_y \geq 1.8$ (see also Fig. 8, where $R_y/R_x = 1.92$). For $R_y/R_x \leq 1.5$, two step transitions in the $\langle v\rangle(F_L)$ curves are always seen. The onset of vortex motion also appears to be strongly dependent on the ratio R_y/R_x. As long as $R_y > R_x$, the critical current is higher when $\mathbf{F}_L \parallel \mathbf{x}$. When $R_y < R_x$, the highest critical current is found for $\mathbf{F}_L \parallel \mathbf{y}$.

When $\mathbf{F}_L \parallel \mathbf{y}$, the important length scale determining the confinement of the trapped vortices is the width R_x of the rectangular blind antidots. Since R_x is kept constant in the calculations, we indeed expect to find no dependence of the $\langle v\rangle(F_L)$ transitions on R_y/R_x.

When $\mathbf{F}_L \parallel \mathbf{x}$, on the other hand, the initial critical depinning force is very sensitive to R_y, because now this parameter determines the confinement of the vortices. When $R_y/R_x = 0$, i.e. $R_y = 0$, the pinning centers are in fact points in the x-direction, which results in a very low threshold value for the initial vortex depinning transition. When R_y/R_x increases, the vortices trapped in the rectangular blind antidots obtain more freedom to shift their positions along the y-axis. This gradually improves their ability to reduce the strain arising from the vortex-vortex interaction in an incommensurate row. In this way, the initial vortex depinning of the incommensurate rows can be delayed to higher F_L.

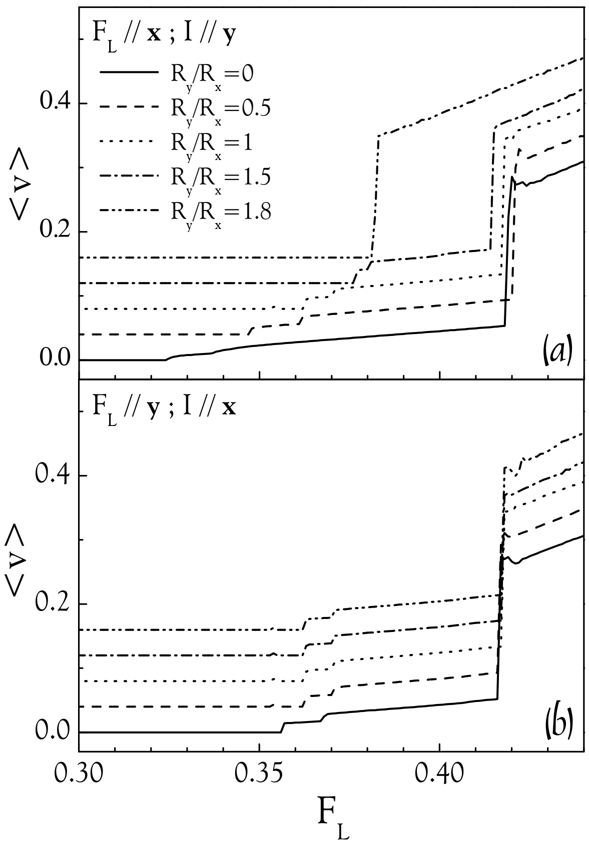

FIG. 10: Average vortex velocity as a function of the Lorentz force $\mathbf{F}_L$ at $H/H_1 = 0.8$ with $\mathbf{F}_L \parallel \mathbf{x}$ (a) and $\mathbf{F}_L \parallel \mathbf{y}$ (b). $R_x = 0.4d$ is kept fixed and the ratio R_y/R_x is varied from 0.0 to 1.8, as indicated.

C. Summary

We have investigated numerically vortex pinning and dynamics in a square array of rectangular blind antidots for different orientations of the applied current or Lorentz force. We demonstrate that the onset of vortex motion, and therefore the critical current, depends on the orientation of the Lorentz force. The critical current is found to be higher when the current is applied parallel to the long side of the antidots. By shifting their position inside the blind antidot, the vortices are able to delay the depinning of the incommensurate vortex rows to higher F_L, by reducing the strain arising from the vortex-vortex interaction in the incommensurate rows. We have also found a strong dependence of the $\langle v\rangle(F_L)$ transition on the aspect ratio of the rectangular blind antidots.

IV. COMPARISON OF THE ANTIDOT AND THE BLIND ANTIDOT SYSTEM

This paper presents results on the anisotropy in vortex pinning for two very different systems: a superconducting film with a square array of rectangular antidots, and with a square array of rectangular *blind* antidots. We have shown that in both systems the critical current is higher and the IV-transition is sharper when the current is sent parallel to the long side of the antidots. On the other hand, a current along the short side of the rectangular antidots yields a lower critical current and a broad IV-transition in both systems.

Although the behavior of the antidot and blind antidot system appears to be similar, the mechanisms determining this behavior are very different in the two systems. In the case of the superconducting film with rectangular *antidots*, the experiments show that the pinning force of the rectangular antidots is identical for the two perpendicular directions. Here, the *vortex-vortex interaction* is found to be anisotropic and responsible for the observed anisotropy in the critical current measurements. In the case of rectangular *blind antidots*, the vortex-vortex interaction is isotropic. Here, the anisotropy in the shape of the antidots and the fact that a vortex can move around freely within the blind antidot cause the anisotropy in the critical current.

V. CONCLUSION

We have investigated vortex pinning and dynamics in superconducting films with a square array of rectangular antidots and blind antidots. As shown by experiments (on the antidots system) and numerical calculations (on both systems), the critical current is higher when applied parallel to the long side of the antidots. For this current direction, we also find sharper IV transitions in both systems. By examining the vortex trajectories after depinning by means of numerical simulations, we were able to demonstrate that the origin of the anisotropy is very different in the antidot and the blind antidot system. Nevertheless, both systems illustrate how patterning of an otherwise isotropic superconducting film, can induce an important anisotropy in the critical current and IV characteristics.

Acknowledgements

This work was supported by the ESF "Vortex" Program, the bilateral BIL 00/02 China/Flanders Project, the Belgian Interuniversity Attraction Poles (IUAP), the Flemish GOA and FWO Programs, and the National Natural Science Foundation of China, the Ministry of Science and Technology of China (nkbrsf-g1999064602). We wish to thank M. J. Van Bael, Y. Bruynseraede, C. Reichhardt, C. J. Olson and F. Nori for helpful discussions.

---

[1] A. F. Hebard, A. T. Fiory, and S. Somekh, IEEE Trans. Magn. **1**, 589 (1977).

[2] M. Baert, V. V. Metlushko, R. Jonckheere, V. V. Moshchalkov, and Y. Bruynseraede, Phys. Rev. Lett. **74**, 3269 (1995).

[3] V. V. Moshchalkov, M. Baert, V. V. Metlushko, E. Rosseel, M. J. Van Bael, K. Temst, R. Jonckheere, and Y. Bruynseraede, Phys. Rev. B **54**, 7385 (1996).

[4] V. V. Moshchalkov, M. Baert, V. V. Metlushko, E. Rosseel, M. J. Van Bael, K. Temst, R. Jonckheere, and Y. Bruynseraede, Phys. Rev. B **57**, 3615 (1998).

[5] A. Castellanos, R. Wördenweber, G. Ockenfuss, A. v.d. Hart, and K. Keck, Appl. Phys. Lett. **71**, 962 (1997).

[6] M. J. Van Bael, K. Temst, V. V. Moshchalkov, and Y. Bruynseraede, Phys. Rev. B **59**, 14674 (1999).

[7] J. I. Martín, M. Vélez, J. Nogués, and I. K. Schuller, Phys. Rev. Lett. **79**, 1929 (1997).

[8] Y. Otani, B. Pannetier, J. P. Nozières, and D. Givord, J. Magn. Magn. Mater. **121**, 223 (1993).

[9] M. J. Van Bael, J. Bekaert, K. Temst, L. Van Look, V. V. Moshchalkov, Y. Bruynseraede, G. D. Howells, A. N. Grigorenko, S. J. Bending, and G. Borghs, Phys. Rev. Lett. **86**, 155 (2001).

[10] D. J. Morgan and J. B. Ketterson, Phys. Rev. Lett. **80**, 3614 (1998).

[11] C. Reichhardt, G. T. Zimányi, and N. Grønbech-Jensen, Phys. Rev. B **64**, 14501 (2001).

[12] M. Tinkham, *Introduction to Superconductivity* (McGraw Hill, New York, 1975).

[13] P.-G. de Gennes, *Superconductivity of Metals and Alloys* (Benjamin, New York, 1966).

[14] A. Wahl, V. Hardy, J. Provost, C. Simon, and A. Buzdin, Physica C **250**, 163 (1995).

[15] J. Evetts (ed.), *Concise Encyclopedia of Magnetic and Superconducting Materials* (Pergamon Press, Oxford, 1992).

[16] P. Martinoli, Phys. Rev. B **17**, 1175 (1978).

[17] O. Daldini, C. Leemann, and P. Martinoli, Solid State Commun. **16**, 509 (1975).

[18] C. Reichhardt and N. Grønbech-Jensen, Phys. Rev. B **63**, 054510 (2001).

[19] A. Buzdin and M. Daumens, Physica C **294**, 257 (1998).

[20] C. Reichhardt, C. J. Olson, and F. Nori, Phys. Rev. Lett. **78**, 2648 (1997).

[21] M. A. Itzler and P. M. Chaikin, Physica B **222**, 260 (1996).

[22] B. Y. Zhu, J. Dong, and D. Y. Xing, Phys. Rev. B **57**, 5063 (1998).

[23] B. Y. Zhu, L. V. Look, V. V. Moshchalkov, B. R. Zhao, and Z. X. Zhao, Phys. Rev. B **64**, 012504 (2001).

[24] A. Brass and H. J. Jensen, Phys. Rev. B **39**, 9587 (1989).

[25] A. Brass and H. J. Jensen, Phys. Rev. B **41**, 6394 (1990).

[26] S. B. Field, S. S. James, J. Barentine, V. Metlushko, G. Crabtree, H. Shtrikman, B. Ilic, and S. R. J. Brueck, Phys. Rev. Lett. **88**, 67003 (2002).

[27] S. J. Bending, A. N. Grigorenko, R. G. Humphreys, M. J. Van Bael, J. Bekaert, L. Van Look, V. V. Moshchalkov, and Y. Bruynseraede, Physica C **341-348**, 981 (2000).

[28] K. Harada, O. Kamimura, H. Kasai, T. Matsuda, A. Tonomura, and V. V. Moshchalkov, Science **274**, 1167 (1996).

[29] A. Bezryadin and B. Pannetier, J. Low Temp. Phys. **102**, 73 (1996).